

Observation and estimation of Lagrangian, Stokes and Eulerian currents induced by wind and waves at the sea surface

FABRICE ARDHUIN¹, LOUIS MARIÉ², NICOLAS RASCLE², PHILIPPE FORGET³, AND AARON ROLAND⁴

¹*Service Hydrographique et Océanographique de la Marine, Brest, France*

²*Ifremer, Brest, France*

³*Laboratoire de Sondages Electromagnétiques de l'Environnement Terrestre, LSEET, Université du Sud Toulon-Var, France*

⁴*Institut für Wasserbau und Wasserwirtschaft, Technische Universität Darmstadt, Germany*

(Manuscript received October 2008, in final form)

ABSTRACT

The surface current response to winds is analyzed in a two-year time series of a 12 MHz (HF) Wellen Radar (WERA) off the West coast of France. Consistent with previous observations, the measured currents, after filtering tides, are of the order of 1.0 to 1.8% of the wind speed, in a direction 10 to 40 degrees to the right of the wind, with systematic trends as a function of wind speed. This Lagrangian current can be decomposed as the vector sum of a quasi-Eulerian current U_E , representative of the top 1 m of the water column, and part of the wave-induced Stokes drift U_{ss} at the sea surface. Here U_{ss} is estimated with an accurate numerical wave model, thanks to a novel parameterization of wave dissipation processes. Using both observed and modelled wave spectra, U_{ss} is found to be very well approximated by a simple function of the wind speed and significant wave height, generally increasing quadratically with the wind speed. Focusing on a site located 100 km from the mainland, the wave induced contribution of U_{ss} to the radar measurement has an estimated magnitude of 0.6 to 1.3% of the wind speed, in the wind direction, a fraction that increases with wind speed. The difference U_E of Lagrangian and Stokes contributions is found to be of the order of 0.4 to 0.8% of the wind speed, and 45 to 70 degrees to the right of the wind. This relatively weak quasi-Eulerian current with a large deflection angle is interpreted as evidence of strong near-surface mixing, likely related to breaking waves. Summer stratification tends to increase the U_E response by up to a factor 2, and further increases the deflection angle of U_E by 5 to 10 degrees. At locations closer to coast, U_{ss} is smaller, and U_E is larger with a smaller deflection angle. These results would be transposable to the world ocean if the relative part of geostrophic currents in U_E were weak, which is expected. This decomposition into Stokes drift and quasi-Eulerian current is most important for the estimation of energy fluxes to the Ekman layer.

1. Introduction

Surface drift constitutes one of the most important applications of the emerging operational oceanography systems (e.g. Hackett et al. 2006), and plays an important role in larvae recruitment and ocean biogeochemistry. A quantitative understanding of the relative contribution of the wave-induced Stokes drift to the near surface velocities is also paramount for the proper estimation of air-sea energy fluxes. The quantitative variation of surface drift as a function of the forcing parameters is still relatively poorly known. In areas of strong currents due to tides or quasi-geostrophic dynamics, the surface drift current is highly correlated to the sub-surface current. Otherwise, winds play a major role in defining the surface velocities.

Recent theoretical and numerical works (Ardhuin et al. 2004; Rascle et al. 2006; Ardhuin et al. 2008c) have sought to reconcile historical measurements of Eulerian and Lagrangian (i.e. drift) velocities with recent knowledge on wave-induced mixing (Agrawal et al. 1992) and wave-induced drift (Rascle et al. 2008). These suggest that the surface Stokes drift U_{ss} induced by waves typically accounts for 2/3 of the surface wind-induced drift, in the open ocean, and that the surface wind-related Lagrangian velocity $U_L(z)$ is the sum of the strongly sheared Stokes drift $U_S(z)$ and a relatively uniform quasi-Eulerian current $\hat{u}(z)$, defined by Jenkins (1987) and generalized by Ardhuin et al. (2008c). The Stokes drift decays rapidly away from the surface on a scale which is the Stokes depth D_S . For deep-water monochromatic waves of wavelength L , $D_S = L/4$ and the Stokes drift is reduced to 4% of its surface value at that depth. For random waves a similar result requires a more com-

Corresponding author address: Fabrice Ardhuin, Service Hydrographique et Océanographique de la Marine, 29609 Brest, France
E-mail: ardhuin@shom.fr

plex definition, but the approximate same result can be obtained by using the mean wavelength $L_{03} = gT_{m03}^2$ where T_{m03} is the mean period defined from the third moment of the wave frequency spectrum (see Appendix).

For horizontally homogeneous conditions, the depth-integrated quasi-Eulerian mass transport vector \mathbf{M}^m is constrained by the balance between the Coriolis force and the wind (τ_a) and bottom (τ_b) stresses (Hasselmann 1970; Ardhuin et al. 2004; Smith 2006),

$$\frac{\partial \mathbf{M}^m}{\partial t} + (\mathbf{M}^m + \mathbf{M}^w) \times \mathbf{e}_z = \tau_a - \tau_b, \quad (1)$$

where \mathbf{M}^w is the (Stokes) mass 'transport'¹ induced by surface gravity waves, f is twice the vertical component of the Earth rotation vector, usually called the 'Coriolis parameter', and \mathbf{e}_z is the vertical unit vector, pointing up. The surface stress vector τ_a is typically of the order of $\rho_a C_d U_{10}^2$ with ρ_a the air density and C_d in the range $1-2 \times 10^{-3}$ and U_{10} the wind speed at 10 m height. The horizontal homogeneity is obviously never achieved strictly (e.g. Pollard 1983), and this aspect will be further discussed in the context of our measurements.

The wind-driven current is not expected to be significant at a depth greater than 0.7 times the Ekman depth $D_E = 0.4 \sqrt{(\tau_a / \rho_w) / f}$ (i.e. less than 0.2% of the wind speed if the surface value is 2.8% of U_{10} , Madsen 1977). For a wind speed $U_{10} = 10 \text{ m s}^{-1}$, $0.7 D_E$ is of the order of 30 m. In locations with a larger water depth, the bottom stress is thus expected to be negligible. Further, this depth of maximum influence can also be limited by a vertical stratification, with larger velocities in shallow mixed layers, and directions of U_E more strongly deflected to the right of the wind (in the Northern Hemisphere) than previously expected (Price and Sundermeyer 1999; Raschle 2007). It has also been proposed by Polton et al. (2005) that the wave-induced mass 'transport' M^w may play a role in the modification of near-surface currents, but M^w is generally less than 30% of the Ekman transport $M^E = \tau_a / f$, and its effect appears to be secondary compared to the stratification (Raschle and Ardhuin 2009). The time-averaged balance given by (1) is thus approximately, $\mathbf{M}^m = -\mathbf{M}^w + (\tau_a \times \mathbf{e}_z) / f$. This was nearly verified for the LOTUS3 dataset (Price and Sundermeyer 1999), when allowing for wave-induced biases in the mooring measurements (Raschle and Ardhuin 2009). Yet, this is not always the case (e.g. Nerheim and Stigebrandt 2006), possibly due to baroclinic currents and other phenomena that are difficult to separate from the wind-driven component.

The vertical profile of the quasi-Eulerian current is, under the same homogeneous and stationary circumstances, the solution of (Xu and Bowen 1994; Ardhuin et al.

2008c)

$$\frac{\partial \hat{\mathbf{u}}}{\partial t} + (\hat{\mathbf{u}} + \mathbf{u}_S) \times \mathbf{e}_z = \frac{\partial}{\partial z} \left(K \frac{\partial \hat{\mathbf{u}}}{\partial z} \right), \quad (2)$$

where K is a turbulent mixing coefficient.

These predictions were verified by Raschle (2007) with mooring data at depths greater than 5 m and surface-following measurements by Santala and Terray (1992) at depths larger than 2 m. When extrapolated to the surface using a simple numerical model, these observations give directions of U_E between 45° and 90° , more than the 45° given by the constant eddy viscosity model of Ekman (1905), as extended by Gonella (1971), and the 10° given by the linear eddy viscosity model of Madsen (1977). This surface angle, and the magnitude of U_E is also critical for the estimation of the flux of wind energy to the Ekman layer (e.g. Wang and Huang 2004), or the analysis of near-surface drifter data, which often does not take into account the wave-induced motion (e.g. Rio and Hernandez 2003; Elipot and Lumpkin 2008). It is thus necessary to measure ocean velocities much closer to the surface.

High Frequency (HF) radars can provide such measurements, at depths that depend on their operating frequency. Using a 30 MHz radar, Mao and Heron (2008) made observations that are also consistent with the idea that the drift current, found to be 2.1% of the wind speed on average, is the sum of U_E which, according to their theory, depends quadratically on the wind speed, and U_{ss} which they estimate to depend linearly on the wind speed, with a variation according to the fetch. Unfortunately, their analysis relied on empirical wave estimates that give large relative errors (of the order of 100%, see e.g. Kahma and Calkoen 1992; Ardhuin et al. 2007), and a limited range of wind speeds. Other HF-radar observations give a surface current of the order of 1.5 to 2.5% of U_{10} (Essen 1993) with 25 to 30 MHz radars. Dobson et al. (1989) also report a ratio of 2.0% using a 22 MHz radar, and Shay et al. (2007) report a ratio of 2 to 3% using a 16 MHz radar in water depths of 20 to 50 m. These analyses are very difficult to interpret due to the filters applied on time series to remove motions (tides, geostrophic currents ...) that are not related to the wind, and also because of the importance of inertial oscillations that make the wind- and wave-driven current a function of the full wind history, and not just a function of the wind vector at the same time and location.

In the present paper we extend the previous analyses of HF radar data by independently estimating the Stokes drift, using an accurate wave model. We find that at our deep water² North-East Atlantic site the quasi-Eulerian current U_E is of the order of 0.6% of the wind speed with a direction that is, on average, 60° to the right of the wind. We also find that the time-dependent response of surface

¹Because in the momentum balance (1) the term \mathbf{M}^w drives a component of mean transport that opposes \mathbf{M}^w , there is no net wave-induced transport, except in non-stationary or non-homogeneous conditions Hasselmann (1970); Xu and Bowen (1994).

²This means deeper than both the Stokes depth D_S and the expected Ekman depth D_E .

current to the wind is typical of a slab layer with a transfer function proportional to $1/(f + \omega)$, where ω is the radian frequency considered. This result is expected to be representative of the open ocean. Therefore the estimates of the flux of wind energy to the Ekman layer by e. g. Wang and Huang (2004) may not be quantitatively correct: they used an angle of 45° , a surface velocity which is $2\sqrt{\tau_a/\rho_w}$ for steady winds (about 0.2% of the wind speed), and a transfer function proportional to $1/\sqrt{f + \omega}$. A proper analysis of the effects of waves is needed to properly evaluate energy fluxes.

Our new data and its processing are described in section 2, and the analysis of the stratification effect is presented in section 3 with conclusions in section 4.

2. Lagrangian and quasi-Eulerian current from HF radars

a. Radar measurements and processing

High frequency radars measure, among other things (e.g. Ivonin et al. 2004), the phase velocity C of Bragg waves that have a wavelength equal to one half of the radar electromagnetic wavelength and that propagate in directions away from and toward the radar. This phase velocity is a combination of the quasi-Eulerian current U_E (Stewart and Joy 1974; Kirby and Chen 1989), the phase speed of linear waves C_{lin} , and a nonlinear wave correction (Weber and Barrick 1977) that can be interpreted as a filtered surface Stokes drift U_{Sf} . For monostatic systems, the usual radial current velocity in the direction θ_B towards one radar can be expressed as

$$\begin{aligned} U_R(\theta_B) &= C(\theta_B) - \mathbf{C}_{lin} \cdot \mathbf{e}_{\theta_B} \\ &= U_{Sf}(\theta_B) + \mathbf{U}_E \cdot \mathbf{e}_{\theta_B}, \end{aligned} \quad (3)$$

where \mathbf{e}_{θ_B} is the unit vector in direction θ_B . This velocity can be loosely interpreted as the projection in direction θ_B of a current vector \mathbf{U}_R . The reason why this is not exactly true is that $U_{Sf}(\theta_B)$ for all directions cannot be exactly given by the projection of a vector \mathbf{U}_{Sf} . In other words, $U_{Sf}(\theta_B)$ is not exactly proportional to $\cos(\theta_B)$, although it is a reasonable approximation (Broche et al. 1983).

In order to express U_{Sf} , we first define the Stokes drift vector for waves with frequencies up to f_c from the directional wave spectrum $E(f, \theta)$,

$$\mathbf{U}_{ss}(f_c) = 4\pi \int_0^{f_c} \int_0^{2\pi} f \mathbf{k}(f, \theta) E(f, \theta) df, \quad (4)$$

where $k(f)$ is the wave number, equal to $(2\pi f)^2/g$ for linear waves in deep water, and g is the acceleration of gravity. Starting from the full expression given by Weber and Barrick (1977), Broche et al. (1983) showed that the filtered Stokes drift component that affects the radial current measured by one radar station is well ap-

proximated by

$$\begin{aligned} U_{Sf}(k_B, \theta_B) &\simeq \mathbf{U}_{ss}(f_B) \cdot \mathbf{e}_{\theta_B} \\ &+ 4\pi k_B \int_{f_B}^{\infty} \int_0^{2\pi} f \cos(\theta - \theta_B) E(f, \theta) d\theta df \end{aligned} \quad (5)$$

where f_B is the frequency of the Bragg waves, and \mathbf{k}_B is the corresponding wavenumber vector, with a direction θ_B and magnitude k_B . The full expression, correcting typographic errors in Broche et al. (1983) is given in Appendix A. In order to simplify the notations, the variable k_b in U_{Sf} will now be omitted, but the filtered Stokes drift is always a function of the Bragg wavenumber, thus being different for different radar frequencies.

The depth-varying quasi-Eulerian current $\hat{u}(z)$ is defined as the difference of the Lagrangian velocity and Stokes drift (Jenkins 1987), and can generally be estimated from the full velocity field using a Generalized Lagrangian Mean (Ardhuin et al. 2008c). The value U_E estimated from the radar is, according to linear wave theory, the integral of $\hat{u}(z)$ weighted by the Bragg wave Stokes drift profile (Stewart and Joy 1974; Kirby and Chen 1989). In deep water this is,

$$U_E = 2k_B \mathbf{e}_{\theta_B} \cdot \int_{-\infty}^0 \hat{u} e^{2k_B z} dz. \quad (6)$$

Here we use data from a WERA HF-radar system (Gurgel et al. 1999), manufactured by Helzel GmbH, and operated at 12.4 MHz. The Bragg wavelength is 12.1 m, corresponding to a wave frequency of 0.36 Hz in deep water. Thus half of the weight $e^{2k_B z}$ in eq. (7) comes from water depths less than 0.6 m from the moving sea surface, compared to 0.28 m with the 30 MHz radar of Mao and Heron (2008). The relative contributions from deeper layers to U_E decrease exponentially with depth as $\exp(2k_B z)$. Therefore U_E can be interpreted as the quasi-Eulerian current in the top 1 m of the ocean.

The radar system has been deployed and operated by Actimar SAS, since July 2006 on the west coast of France (figure 1), measuring surface currents and sea states every 20 minutes. The area is characterized by intense tidal currents, in particular between the largest islands where it exceeds 3 m s^{-1} during mean spring tides. Also important, the offshore stratification is largely suppressed by mixing due to the currents in the areas shallower than 90 m, resulting in complex temperature fronts that are related to the bottom topography (e.g. Mariette and Le Cann 1985).

Each radar station transmits a chirped continuous wave with a repetition frequency of 4 Hz and a 100 kHz bandwidth which gives a radial resolution of 1.5 km. The receiving antennas are 16-element linear arrays with a spacing of 10 m, giving a typical angular resolution of 15 degrees. The raw data is processed to remove most of the interference signals (Gurgel and Barbin 2008). Ensemble-averaging over 4 consecutive segments of 512 pulses

yields a velocity resolution $d_u = 0.09$ m/s in the Doppler spectrum used to estimate each individual radial current measurement. Yet, the current value is obtained by a weighted sum over a 9-point window applied to the Doppler spectrum. Provided that some inhomogeneity exists in the current field, the width of the Doppler spectrum permits a measurement resolution that is infinitely small, but with an accuracy that is difficult to define, because no other instrument, except maybe for the CODE-type drifter (Davis 1985), is able to measure surface current in the top one meter of the ocean. Similarly, satellite altimeters are reported to measure the mean sea level position with an accuracy of the order of 2 cm whereas their typical range resolution is close to 40 cm. Prandle (1987) used the coherence of the tidal motions to infer that the accuracy of his 27 MHz radar system was indeed less than the Doppler resolution when averaged over one hour. We will thus take the accuracy to be equal to the resolution, but as it will appear below, the only source of concern for our analysis is not so much the random error but a systematic bias, since we will average a very large number of independent measurements.

Because we investigate the relationship between surface currents and winds based on modelled winds and waves, we will consider only the temporal evolution of the wave field at one point of the radars' field of view that is representative of the offshore conditions, at a distance of 80 to 100 km from shore and with a water depth of 120 m. The reason for choosing this location is that we have verified the wind and wave model results to be most accurate offshore where they were verified in situ with measurements that only span 6 and 9 months of our radar time series. Other reasons for looking at offshore conditions are the expected limited effect of the bottom, and the expected small horizontal gradients of both tidal currents and other processes. Namely, we stay away from the thermal front that typically follows the 90 m depth contour (Mariette and Le Cann 1985; Le Boyer et al. 2009). The down side of this choice is that the HF-derived current is generally less accurate as the distance from the coast increases, and the coverage is not permanent, especially during severe storms (e.g. figure 1). These two drawbacks are limited in practice, as we now discuss.

Interferences and ships cause some data to be rejected in the radar processing, or yield bad measurements, and heavy seas or calm seas also reduce the working radar range. In order to obtain a nearly continuous time series, we compiled and filtered data from a 0.2° in latitude by 0.3° in longitude box around that point (A in figure 1, the arrow spacing indicate the resolution of the radar grid). This compilation was done in two steps. First, based on a visual inspection of the data, at each radar grid point 0.05% of the total number of data points in the radial velocities time-series are considered spurious and removed. These points are selected as the points where the raw radial current time-series differs most from the result of a 3-points median filter. The 0.05% value was selected as a convenient rule-of-thumb, which permits the removal of

most of the visibly spurious points, but does not introduce too many unnecessary gaps in the time-series. Second, the time-series of all the grid points in the box around A were converted to u and v components and averaged.

The Cartesian components of \mathbf{U}_R and \mathbf{U}_E with respect to west-east (component u) and south-north (v) directions are calculated from the two radial components $U_R(\theta_{B1})$ and $U_R(\theta_{B2})$, each measured by one radar station, before and after the subtraction of $U_{sf}(\theta_B)$. These Cartesian components suffer from a geometrical dilution of precision (GDOP), varying with position (Chapman et al. 1997; Shay et al. 2007). The radar beams intersect at point A with an angle $r = 34^\circ$ and it is possible to estimate the GDOP values for u and v , i.e. the ratios S_u/s and S_v/s where S_u , S_v and S are the uncertainties in u , v and u_r , respectively. Assuming that S has no bias and is uniformly distributed from $-d_u/2$ to $+d_u/2$, each radar measurement has an intrinsic uncertainty $S_u = 0.04$ m s $^{-1}$ and $S_v = 0.11$ m s $^{-1}$.

This compiled time series, extending from July 5 2006 to July 31 2008, is the basis of the following analysis. The 1200 s resolution data was averaged over 3 h blocks centered on round hours. Gaps shorter than 6 h were linearly interpolated. That time series is 97% complete, and thus covers two full years. Other parts of the radar field of view yield similar results, briefly discussed below. Due to the averaging in space and time, each point in the time series is the combination of about 30 range cells and 9 time intervals, i.e. 180 independent velocity measurements when the full radar range is obtained. Even with a 11 cm s $^{-1}$ uncertainty on the original measurement, the expected r.m.s. error on the velocity components are thus less than 1 cm s $^{-1}$. This analysis assumes that the instrument is not biased. After verification of the radar antenna lobe patterns using both in situ transmitters and a novel technique based on the analysis of radio interference (to be described elsewhere), the main lobe of the radar is known to be mispointed by less than 5 degrees, with a -3dB width less than 15° . The largest source of uncertainty is thus the interpretation of the phase speed and the numerical estimation of the Stokes drift, as discussed below.

Because we wish to focus on the random wind-driven currents, we also performed a tidal analysis using the T-TIDE software (Pawlowicz et al. 2002) applied to each velocity component. This analysis on the full time series (before time averaging) allows the removal of the deterministic diurnal constituents K_1 , O_1 , P_1 and Q_1 that have amplitudes of 1.5 to 0.3 cm s $^{-1}$, with estimated errors of 0.1 cm s $^{-1}$. Because this only corrects for 95% of the apparent variance in the M_2 and S_2 semi-diurnal tides, these will be further filtered using a time filter.

b. Numerical wave model and estimations of Stokes drift

1) GENERAL PRINCIPLES

As expressed by eq. (5), the estimation of $U_{sf}(\theta_B)$

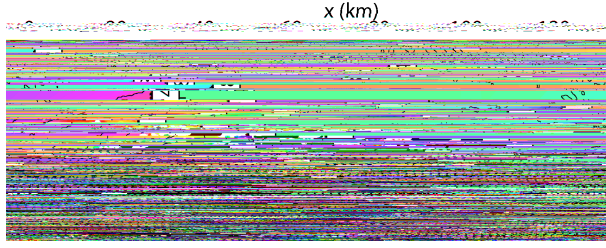


FIG. 1. Map of the area showing a map of significant wave height on January 1st 2008, at 12:00 UTC, estimated with a numerical wave model (see Appendix B), and the instantaneous surface current measured by the H.F. radars installed at Porspoder and Clédén-Cap-Sizun. In situ measurement stations include the weather buoy BEAtrice and the Pierre Noires (62069) directional Datawell waverider buoy (installed from November 2005 to March 2006 and back again since January 2008), and a previous waverider deployment (Iroise), more representative of the offshore wave conditions. The large black square around point A is the area over which the radar data has been compiled to provide the time series analyzed here, representative of offshore conditions. When the radar functionned, over the entire square measurements are available for more than 80% of the 20 minute records, a number than rises to 99% for the area East of $5^{\circ}35'W$. The partial radar coverage around point A is typical of high sea states with $H_s > 6$ m offshore, which are rare events.

requires the measurement or modelling of the wave spectrum $E(f, \theta)$. In situ buoys were moored for restricted periods at several locations for the investigation of offshore to coastal wave transformation (Ardhuin 2006) and to provide complementary data for radar validation. The radar also measures the sea state, but the coverage is often limited, and its accuracy for a 20 minute record is typically only of the order of 25% for the significant wave height H_s . Thus, in order to use the full current time series at the offshore location (point A) we have to estimate the sea state using a numerical wave model.

The model used is an implementation of the WAVEWATCH III code, in its version 3.14 (Tolman 2007, 2008), with minor modifications of the parameterizations,

see appendix B, and the addition of advection schemes on unstructured grids.

The model setting consists of a two-way nested pair of grids, covering the global ocean at 0.5 degree resolution and the Bay of Biscay and English channel at a resolution of 0.1 degree. A further zoom over the measurement area is done using an unstructured grid with 8429 wet points (figure 1). The model setting is fully described in appendix B.

In practice, U_{Sf} is dominated by the first term $U_{ss}(f_B)$, in eq. (5). Examining a large number of spectral data (6 buoys for 2 years spanning a range of wave climates, see appendix C), we realized that $U_{ss}(f_B)$ is essentially a function of the wind speed U_{10} and the wave height H_s . While U_{10} explains typically only 50% of the variance of $U_{ss}(f)$ with $0.3 < f < 0.5$, U_{10} and H_s generally explain over 85% of the variance. This behaviour of $U_{ss}(f)$ is similar to that of the fourth spectral moment, related to the surface mean square slope (Gourrion et al. 2002; Vandemark et al. 2004). The reason for this correlation is that the wind speed is obviously related to the high frequency part of the wave spectrum, which determines most of the Stokes drift, while H_s is a surrogate variable for both the presence of swell and the stage of development of the wind sea. Here we find,

$$U_{ss}(f_c) \simeq 5.0 \times 10^{-4} \left[1.25 - 0.25 \left(\frac{0.5}{f_c} \right)^{1.3} \right] U_{10} \times \min \{ U_{10}, 14.5 \} + 0.025 (H_s - 0.4). \quad (7)$$

The relationship given by eq. (7) appears to be very robust, with a $2.6 \text{ cm}^{-1} \text{ r. m. s.}$ difference compared to global hindcast values of $U_{ss}(\infty)$, which is a 16.9% difference. Nevertheless, when compared to buoy data, an accurate wave model generally provides a better fit to the observations (Appendix C). We thus have used our hindcasts using WAVEWATCH III to provide an estimate for U_{Sf} .

2) UNCERTAINTY ON U_{Sf} AROUND POINT A

We have no wave measurement at point A, and no permanent spectral measurement in the area. A detailed validation of U_{ss} was thus performed for the coastal buoys 62069 (figure 1), 62064 (off Cap Ferret, 600 km to the southeast of point A), the U.S. Northwest Pacific Coast (appendix C), U.S. East coast, Gulf of Mexico and California.

We further use wave information at buoy 62163, located 150 km west of point A, representative of the offshore conditions found at point A, and measured in the area by satellite altimeters. The present model estimates of H_s are more accurate at buoy 62163, located 150 km west of point A, than at Pacific buoy locations. Further, the model estimate of the fourth moment m_4 of the wave spectrum is better correlated in the Bay of Biscay to

radar altimeter C-band cross-section, compared to other regions of the world ocean (Appendix C). We thus expect the model estimate of U_{ss} ($f_B = 0.36$ Hz) to have a bias smaller than 5%, with a random error less than 20% (see Appendix C). As a result, we chose to use this numerical wave model for the estimation of U_{ss} and U_{Sf} . We can thus propose an error budget for our estimate of the wind-driven quasi-Eulerian current in which the measurement error is dominated by U_{Sf} with a bias of 5% at most and a standard deviation less than 20% overall. Using the analysis of 2 years of model results, this standard deviation at the Pacific buoy 46005 is 24% for wind speeds of 3 m s^{-1} , 20% for 5 m s^{-1} , 16% for 7 m s^{-1} , 11% for 11 m s^{-1} . Given the general accuracy of the wave model in the North-East Atlantic, we expect similar results here.

We thus expect that the estimated quasi-Eulerian current U_E at 3 hour intervals is accurate within 0.2% of U_{10} . On this time scale, it is difficult to rule out contributions from horizontal pressure gradients in the momentum balance, and this current may not be purely wind-driven.

The averaged current, e.g. for a given class of wind speed, as shown on figure 7, has a relative accuracy better than 0.1% of U_{10} . In-situ measurements of time-averaged velocities from 10 to 70 m above the bottom at $48^\circ 6' \text{N}$ and $5^\circ 23' \text{W}$ (south of point A, see figure 1) using a RDI Workhorse ADCP deployed from June to September 2007 (Le Boyer et al. 2009) give tide-filtered currents less than 2 cm s^{-1} or 0.25% of the wind speed when averaged following the wind direction (the instantaneous measurements are rotated before averaging), and less than 0.1% when winds stronger than 10 m s^{-1} . This is typically less than 20% of U_{Sf} . Assuming that wind-correlated baroclinic currents are negligible during the ADCP measurement campaign, the wind-correlated geostrophic current is expected to be less than 0.2% of U_{10} . Generalizing this result to the entire radar time series the averaged values of U_E can be interpreted as a wind-driven current with an accuracy to within 0.3% of U_{10} .

3. Analysis of wind-driven flows

The study area is characterized dominated by moderate 6 to 12 m s^{-1} winds, from a wide range of directions, with slightly dominant South-Westerly and North-Easterly sectors (figure 2).

a. Rotary spectral analysis

The rotary spectral analysis gives both the frequency distribution of the signal, and an indication of its circular polarization (Gonella 1971). The positive frequencies correspond to counter-clockwise motions, and the negative frequencies correspond to clockwise motions, the usual polarization of inertial motions in the Northern Hemisphere.

The instantaneous measurements of the radar are dominated by tidal currents, and the variance of motions with

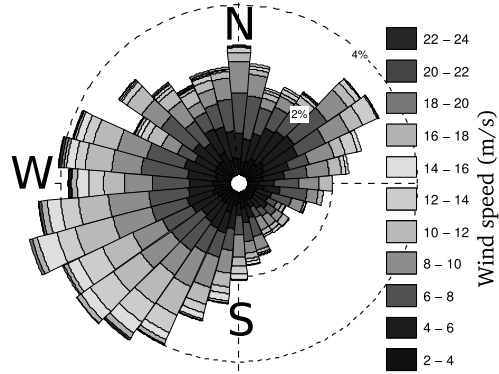


FIG. 2. Wind rose for the years 2006 to 2008 at point A, based on ECMWF analyses. The observations at BEAtrice buoy give a similar result. For each direction, the cumulative frequency is indicated with wind speeds increasing from the center to the outside, with a maximum of 4.3% maximum from West-South-West (heading 250°). An isotropic distribution would have a maximum of 2.7%.

frequencies less than 1.75 count per day (cpd) only accounts for 8% of the total variance (figure 3). These low frequency motions include the diurnal tidal constituents, most importantly K_1 and O_1 , but these only account for 0.1% of the variance. The low frequency motions are generally dominated by near-inertial motions, which are polarized clockwise with frequencies close to the inertial frequency $f_I = 1.3$ counts per day (c.p.d., see figure 3).

b. Co-spectral analysis

Here we investigate the relationship between measured currents, processed as described above, and winds, taken from 6-hourly wind analyses from ECMWF. These analyses were verified to give excellent correlation ($r \simeq 0.92$) with the BEA buoy (WMO code 62052), which unfortunately malfunctioned during large periods of time. The wind and current data are thus completely independent. The wave model was forced by these same winds, and thus the high level of coherence between the predicted Stokes drift and the wind (figure 4) is not surprising.

In order to isolate the wind-correlated dynamics from the shorter (tide) and longer (general circulation) time scales, we first perform a co-spectral analysis of the measured currents with the wind, following the method of Gonella (1971). In order to keep as much data as possible between data gaps, the Fourier transforms are taken over 264 hours, which corresponds to 21 M_2 tidal cycles. The measured currents are significantly coherent with the wind vector over the range -1.75 to 1.75 cpd (figure 4). This coherence is generally reduced when the Stokes component U_{Sf} is subtracted from the radar measurements.

The radar-measured current vectors U_R have stable directions relative to the wind, 20 to 40° to the right for $f > -f_I$, given by their coherence phase (figure 4). The coherence phase of the Stokes drift increases with fre-

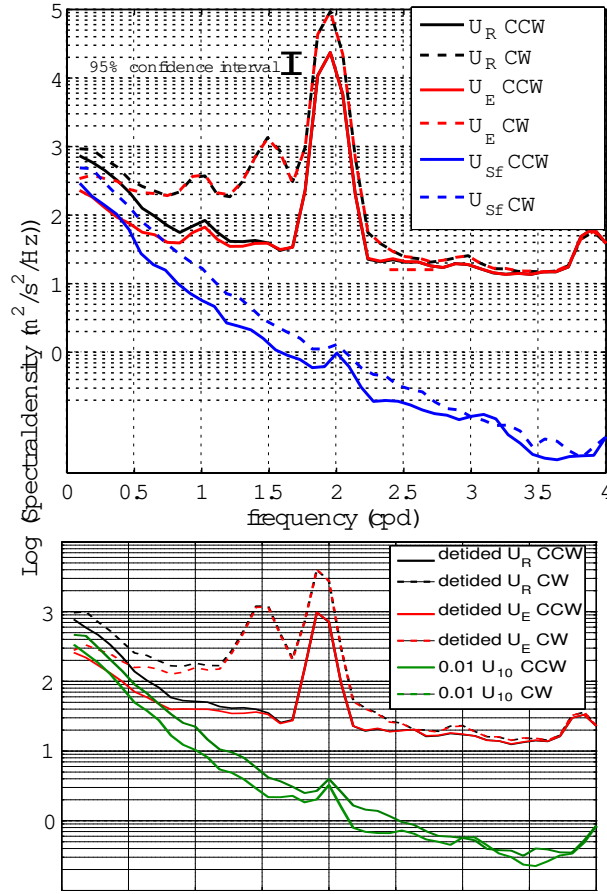


FIG. 3. Rotary power spectra of the current measured by the radar, and the contribution U_{Sf} to the surface Stokes drift estimated via eq. (A1). Clockwise (CW) motions are shown with dashed lines and counter-clockwise motions are shown with solid lines. The spectra were estimated using half-overlapping segments 264 h long over the parts of the time series with no gaps. The number of degrees of freedom is taken to be the number of non-overlapping segments, i.e. 59, at the spectral resolution of 0.09 cpd, giving a relative error of 35% at the 95% confidence level. In the bottom panel the tidal components have been filtered out, which clearly removes the diurnal peak. However, the semi-diurnal tides are only reduced by a factor 25, which is not enough compared to the magnitude of the near-intertidal motions, and requires the use of an additional filter. This tide-filtered time series is used in all of the following.

quency. This pattern is typical of a time lag, that can be estimated to about 1.5 hours, consistent with the relatively slow response of the wave field compared to the current. This is rather short compared to the time scale of wave development, but one should bear in mind that the Stokes drift is mostly due to short waves that respond faster to the wind forcing than the dominant waves. Because the wind preferentially turns clockwise, the Stokes drift is slightly to the left of the wind. The asymmetry in the phase of U_{Sf} for clockwise and counter-clockwise motions may be related to varying fetch when the wind turns.

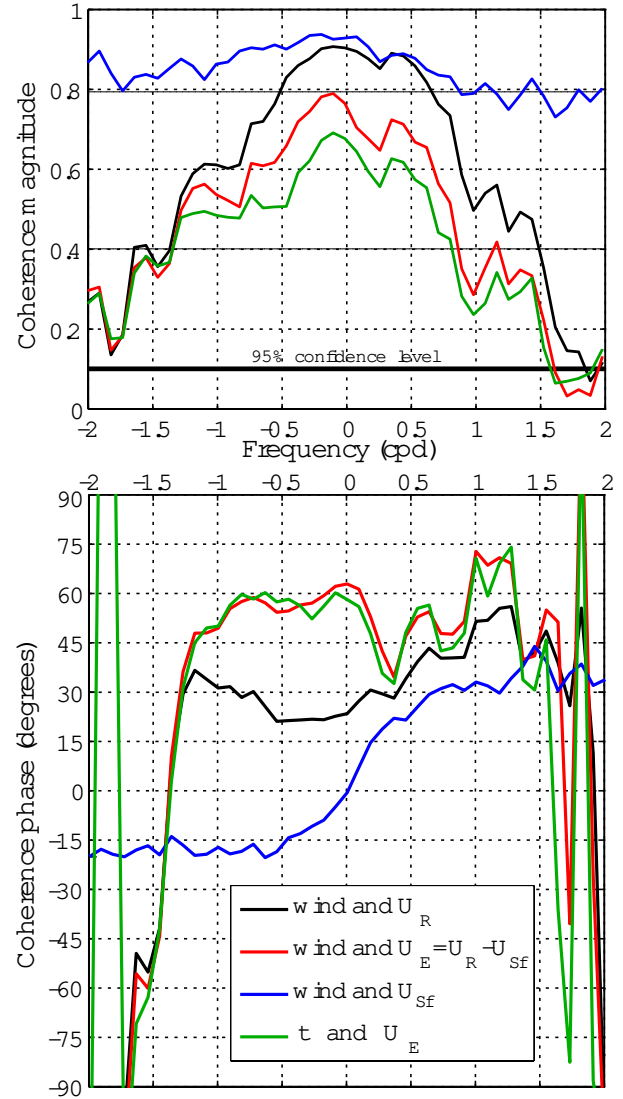


FIG. 4. Rotary co-spectra of the wind and wind stress with the radar-derived current, Stokes drift and Eulerian current. (a) magnitude and (b) phase. The number of degrees of freedom is 108 at the spectral resolution of 0.09 cpd. Coherence is significant at the 95% confidence level for a value of 0.1. Negative and positive frequencies are clockwise and counter-clockwise polarized motions, respectively.

As expected from the theory by Gonella (1972), the phase of the quasi-Eulerian current U_E jumps by about 180° at the inertial frequency $-f_I$. In the frequency range from -1.2 to 0.2 cpd, that contains 40% of the non-tidal signal, U_E is at an angle between 45 and 60° to the right of the wind. This conclusion is not much altered when one correlates the Eulerian current against the wind stress, which, for simplicity is estimated here with a constant drag coefficient, $\tau = 1.3 \times 10^{-3} U_{10} U_{10}$. One may argue that the theoretical filtering of the Stokes drift is not well validated. A lower bound on the estimate of U_{Sf} can be given by removing the contribution from waves shorter

than the Bragg waves. This has very little impact on the estimation of U_E .

The observed coherence phases of U_E and U_{10} are similar to the values given by Gonella (1972, figure 6), based on the constant eddy-viscosity model of Ekman (1905), but for the current considered at a depth as large as 25% of the Ekman depth. Since the radar measurements are representative of the upper 1 meter, and the Ekman depth is generally of the order of 30 m, it follows that the classical Ekman theory, with a constant eddy viscosity, does not apply here. Instead, this large near-surface deflection is consistent with the results obtained with a high surface mixing such as induced by breaking waves (e.g. Mellor and Blumberg 2004; Rascle et al. 2006).

c. Effects of stratification

Following the theory of Gonella (1972) and the previous observations by Price and Sundermeyer (1999), it is expected that the stratification has a significant effect on the surface currents. Here we used sea surface temperature time series to diagnose the presence of a stratification. Because of the strong vertical mixing year-round at the site of buoy 62069, the horizontal temperature difference between points A and point 62069 is a good indicator of the vertical stratification at point A. This temperature difference reaches up to 2°C , and was present in 2006, 2007 and 2008 from early July to late October, as revealed by satellite SST data. We thus separated the data records used for the spectral analysis into "stratified" and "homogeneous" records based on the date of the midpoint in these time series.

These two series show a significant difference (at the 95% confidence level) when the spectra are smoothed over 0.3 c.p.d. bands, with a twice larger response in the cases expected to be stratified (dashed lines, figure 5) for frequencies in the range -1.7 to 1.5 c.p.d. Interestingly the transfer functions decrease from a peak at the inertial frequency as $1/(f + \omega)$ where ω is the radian frequency. This decrease is typical of slab-like behaviors that are expected in mixed layers with a much larger surface mixing (e.g. Rascle et al. 2006) than typically used with Ekman theory, or a mixed layer depth much shallower than the Ekman depth (Gonella 1972). Ekman theory in unstratified conditions, that should apply to our winter and spring measurements, would give a much slower decrease, proportional to $1/\sqrt{f + \omega}$ (Gonella 1972). Together with this stronger amplitude of the current response in stratified conditions, we find a larger deflection angle in the -0.8 to -0.2 c.p.d. frequency range. This pattern of larger currents and larger deflection angles in stratified conditions is consistent with the observations of Price and Sundermeyer (1999), and the numerical model results by Rascle and Ardhuin (2009).

d. Relationship between tide-filtered currents and winds

A proper model for the wind-induced current may be

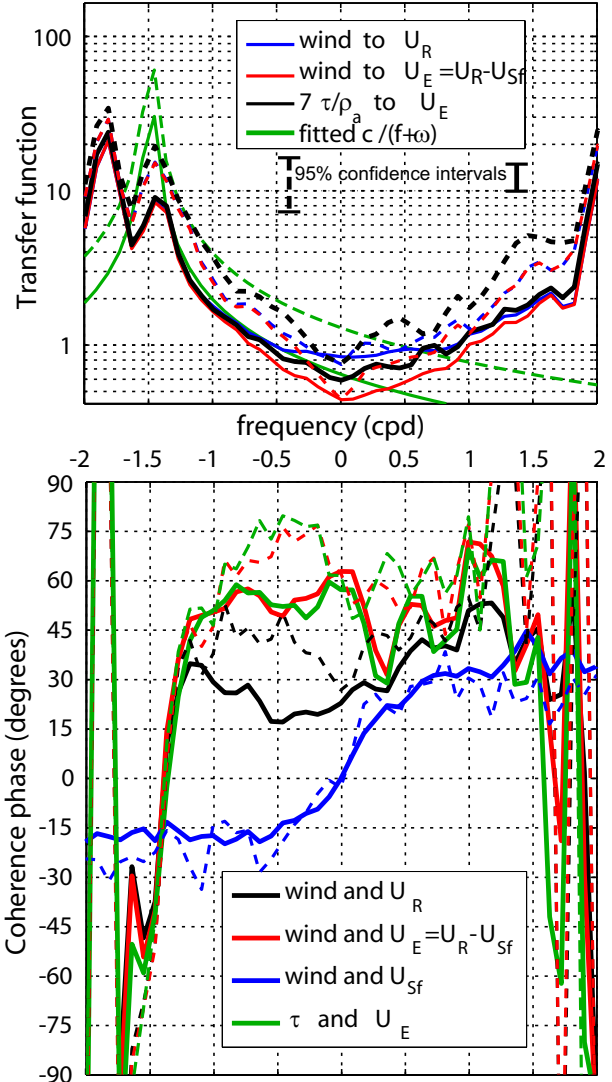


FIG. 5. Amplitude transfer functions (top) and coherence phases (bottom) between the wind forcing and the current response. The dashed lines correspond to records where a stratification is expected to be important (18 out of 108), and the solid lines correspond to the other records. Confidence intervals for the two group of records are shown for the native spectral resolution of 0.09 c.p.d. In order to be at a comparable level the wind stress was multiplied by 50 before estimating the transfer function. The two peaks of the transfer functions at ± 2 cpd are due to the tidal currents but do not correspond to a causal relationship between the wind forcing and the current response.

given by the relationship between the wind speed and wave height, giving the Stokes drift, and the complex transfer function (transfer function and phase) from the wind stress spectrum to the Eulerian current spectrum, following Gonella (1971) or Millot and Crépon (1981), this is beyond the scope of the present paper.

Simpler models that would give the current speed and

direction as a function of the instantaneous wind vector are even less accurate. Because the transfer function is very peaked at the inertial frequency, with a large jump in phase, for a given wind the current speed may vary widely. Yet, for practical reasons, there is a long tradition, for search and rescue operations and ocean engineering applications, of directly comparing current and wind magnitudes and directions. Because of the inertial oscillations, there is usually a large scatter in the correlation of the current and wind speed vectors. In order to compare with previous analyses (e.g. Mao and Heron 2008), we thus perform such a comparison, after filtering out the dominant tidal current, by taking the inverse Fourier transform of the current, wind, and Stokes drift spectra in which the amplitudes of components with frequencies higher than 1.75 cpd, and the zero frequency, are set to zero. Again, the Fourier transforms are taken over 264 hours.

We find that the surface Eulerian U_E current lies 40 to 60° to the right of the wind, suggesting that the near-inertial motions only add scatter to the longer period motions ($|f| < 1.3$ c.p.d.) that were found to have similar deflection angles. Interestingly, the typical magnitude of U_E decreases from about 0.8% of U_{10} at low wind to nearly 0.4% for high winds. This reduction in the relative magnitude of U_E is accompanied by a reduction of the deflection angle from 65° on average for $U_{10} = 3 \text{ m s}^{-1}$ to 40° for $U_{10} = 15 \text{ m s}^{-1}$. On the contrary, the Stokes drift typically increases quadratically with the wind speed. These results contradict the usual result by Kirwan et al. (1979), Mao and Heron (2008), that the Stokes drift should be linear and the Eulerian current should be quadratic in terms of wind speed. The fact that the Stokes drift is quadratic as a function of the wind speed is well shown by observations in figure 6, and the error in Mao and Heron (2008) is likely due to their erroneous assumption that the Stokes drift is dominated by waves at the peak of the spectrum. In the analysis of Kirwan et al. (1979) and Rasche et al. (2006), the error essentially arises from the assumed shape of the wave spectrum.

The less-than-linear dependence of U_E on U_{10} contradicts the usual simple Ekman model for the quasi-Eulerian current, which would predict a current proportional to the wind stress, and thus varying as the square or cube of the wind speed. This difference is likely due to the enhanced mixing caused by breaking waves, which tends to mix the momentum over a scale of the order of the windsea wave height, i.e. increasing with the wind speed (Terray et al. 1996; Rasche et al. 2006). Numerical models without stratification but with a realistic mixing tend to give a quasi-Eulerian current that increases with wind speed and with the inverse wave age. Here the stronger winds do not correspond to very different wave ages, and it is likely that a correlation of deeper mixed layers with stronger winds is the cause of the reduction of U_E with increasing wind speed (Rasche and Arduin 2009). As a result, the nonlinear current response to the

wind stress will likely limit the accuracy of models based on transfer functions.

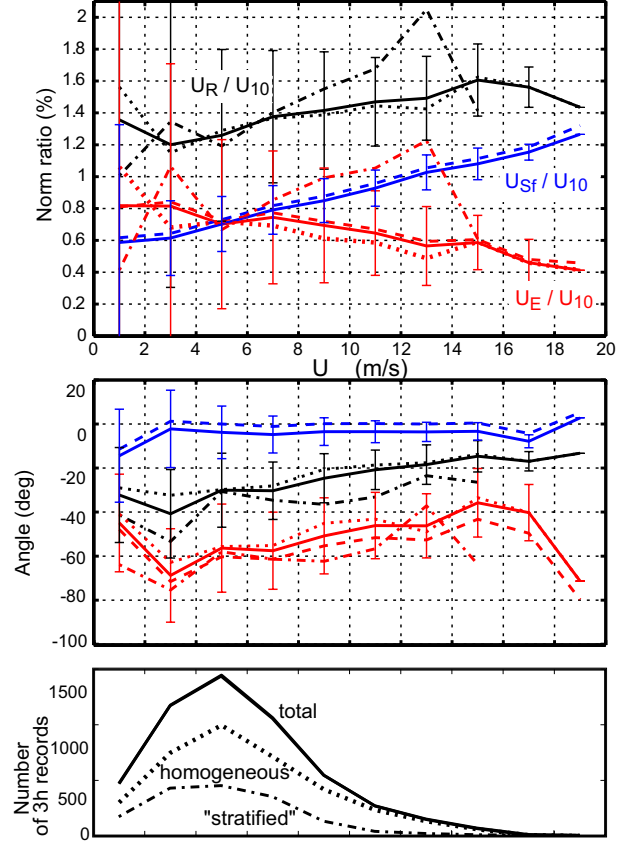


FIG. 6. Observed tide-filtered quasi-Eulerian velocities binned according to wind speed. Dash-dotted lines correspond to stratified conditions only and dotted lines correspond to homogeneous conditions. The number of data records in each of these cases is indicated in the bottom panel. The dashed line shows results when U_{Sf} is replaced by $U_{ss}(f_B)$. Error bars show only 1/2 of the standard deviation for all conditions combined, in order to make the plots readable. All time series (wind, current, U_{Sf} and U_{ss} were filtered in the same manner for consistency (except for the initial de-tiding applied only to the current data). The error bars do not represent measurement errors but rather the geophysical variability due to inertial motions.

e. Effects of fetch or wave development

The same analysis was also repeated for other points in the radar field of view. For example at point B (figure 1), where the radar data quality is generally better, but where the wave model may have a bias of about 10% on U_{ss} , and the ECMWF wind field may be less accurate. Point B is relatively sheltered from Southerly, and North-westerly waves, and the fetch from the East is 40 km at most. If we assume that the winds are accurate at that site too, we find that the radar-derived current is weaker relative to the wind, with U_R/U_{10} typically smaller by 0.2% point (i.e. a $\sim 15\%$ reduction) compared to point A. This appears to be due to a reduction in U_{Sf} , which is

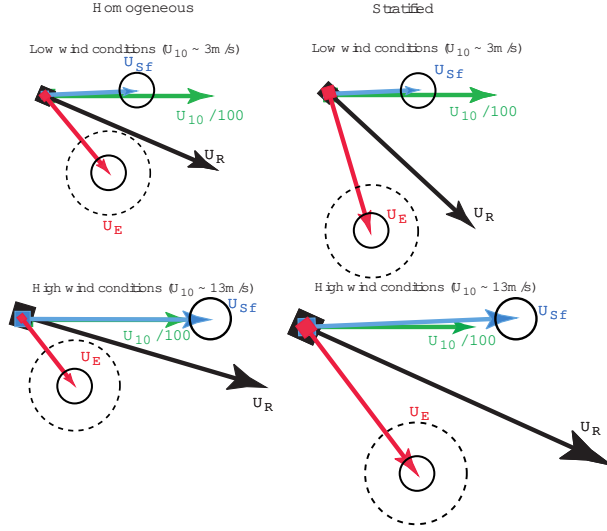


FIG. 7. Mean wind-correlated current vectors in low and high wind conditions, with and without stratification, measured off the West coast of France with the 12.4 MHz HF radar, based on the results shown in figure 6. \mathbf{U}_R is the radar-measured vector, that can be interpreted as a sum of a quasi-Eulerian current \mathbf{U}_E , representative of the upper two meters, and a filtered surface Stokes drift \mathbf{U}_{Sf} . The full surface Stokes drift is typically 40% larger than this filtered value. Solid circles give the expected error on the mean current components due to biases in the wave contribution to the radar measurement. The dashed circle show the expected error on the interpretation of \mathbf{U}_E as a wind-driven current, based on the ADCP measurements at depth of 60 to 120 m, assuming that the baroclinic part of the geostrophic current is negligible.

only partially compensated for by a small increase in U_E . This difference between *A* and *B* nearly vanishes when only Westerly wind situations are considered (defined by winds within 60° from the Westery direction).

4. Conclusions

Using a 2 year time series of HF radar data, and a novel numerical wave model that is shown to reproduce the observed variability of the surface Stokes drift with wind speed and wave height, we have analyzed the wind-driven surface current. When tidal currents are filtered out, we find that the measured velocities are a superposition of a filtered Stokes drift U_{Sf} and a quasi-Eulerian current U_E . With our 12 MHz radar, U_{Sf} is of the order of 0.5 to 1.3% of the wind at 100 km from the coast, the ratio increasing linearly with wind speed. These values are a function of the radar wavelengths and would be larger, by up to 20%, with higher frequency radars that give currents representative of a shallower surface layer. The other component U_E is found to be of the order of 0.6% of the wind speed, and lies, in our Northern Hemisphere, at an average 40 to 70 degrees to the right of the wind, with a large scatter due to inertial oscillations that may be well modelled using a Laplace transform of the wind stress (Broche et al. 1983). This large deflection angle is robustly given by the coherence phase for clockwise motions in the frequency

range from 0 to the inertial frequency.

When instantaneous currents are compared to the wind, the magnitude of U_E appears to decrease with wind speed but it increases when a stronger stratification is expected (figure 6). These surface observations correspond to currents in the depth range 0 to 1.6 m, and confirm previous analysis of deeper subsurface mooring data. If wind-correlated geostrophic current are negligible in our measurements, the shape of the classical picture of the Ekman spiral is not correct, and the surface layer is much more slab-like than assumed in many analyses, probably due to the large wave-induced mixing at the surface (Agrawal et al. 1992). These findings are summarized in figure 7.

If we neglect the wind-correlated geostrophic currents, which we deem reasonable, and interpret U_E as being purely wind-driven, our observations of U_E/U_{10} at point A, are expected to be representative of the open ocean, whereas in coastal areas and small basins, a less developed sea state will lead to a smaller value of U_{Sf} and a larger value of U_E , as we observe at point B. Such a generic relationship of U_E and U_{10} is very important for a proper estimation of the energy flux to the mixed layer. Besides, on top of the wind stress work on the Ekman current, this energy flux should be dominated by the dissipation of wave energy induced by breaking (e.g. Raschle et al. 2008). Also, there is the depth-integrated Stokes-Coriolis force which is equal to the depth-integrated Stokes transport $\mathbf{M}^w = \rho_w \int \mathbf{U}_s(z) dz$, and the Coriolis parameter. This force is smaller than the depth-integrated Coriolis force by about a factor of 3 on average (Raschle et al. 2008), but that may give a comparable work $\rho_w \int \mathbf{U}_s(z) \cdot \hat{\mathbf{u}}(z) dz$ due to the smaller angle between that force and the quasi-Eulerian current $\hat{\mathbf{u}}(z)$. The accurate estimation of the surface Stokes drift using a numerical wave model also opens the way for a more accurate interpretation of space-borne measurements of surface currents using Doppler methods, that are contaminated by a Stokes-like component amplified 10 times or more (Chapron et al. 2005).

Acknowledgments. The efforts of Vincent Mariette and Nicolas Thomas are essential to maintain the radars in proper operating conditions. Funding for the radar purchase and maintenance was provided by DGA under the MOUTON project, and funding for the wave model development was provided under the ECORS project. Florent Birrien performed the integration of Aaron Roland's routines into the WAVEWATCH III framework. Wind and wave data were kindly provided by ECMWF, Météo-France, and the French Centre d'Etudes Techniques Maritimes Et Fluviales (CETMEF), and the sea surface temperature data used to diagnose the presence of a stratified layer was taken from the ODYSSEA Level 4 global analysis product, produced as part of the MERSEA Integrated Project. The SHOM buoy deployments were managed by David Corman with precious help from Guy Amis.

APPENDIX A Nonlinear correction for the wave dispersion relation in a random sea state

Based on the lowest order approximate theory of Weber and Barrick (1977) for deep water waves with $f \simeq 2\pi\sqrt{gk}$, the nonlinear correction to the phase speed of components with wavenumber k_B and direction θ_B , can be expressed as an integral over the wave spectrum. Defining $x = k/k_B$ and $\alpha = \theta - \theta_B$, (Broche et al. 1983, their eq. A2) give the following expression,

$$U_{Sf}(k_B, \theta_B) = \frac{\sqrt{g}}{2} k_B^{3/2} \int_0^\infty \int_0^{2\pi} F(x, \alpha) E(f, \theta) d\theta df,$$

where, correcting for typographic errors, and using $y = x^{1/2} = f/f_B$ and $a = \cos \alpha$,

$$\begin{aligned} F(x, \alpha) &= y \{2a - y + 3xa\} \\ &+ y \sum_{\varepsilon=\pm 1} \frac{\varepsilon - a}{a_\varepsilon - (1 + \varepsilon y)^2} \\ &\times \left\{ (ya - x) \left(a_\varepsilon + (1 + \varepsilon y)^2 \right) / 2 \right. \\ &\left. + (1 + \varepsilon y) (1 + \varepsilon xa + \varepsilon y (x + \varepsilon a) - a_\varepsilon) \right\}, \end{aligned} \quad (\text{A1})$$

with

$$a_\varepsilon = (1 + x^2 + 2\varepsilon xa)^{1/2}. \quad (\text{A2})$$

These expressions give the correct figures in Broche et al. (1983). For $x < 1$ one finds that $F(x, 0) = 4x^{3/2}$, and for $x > 1$, $F(x, 0) = 4x^{1/2}$, as previously given by Longuet-Higgins and Phillips (1962), Huang and Tung (1976) and Barrick and Weber (1977). As commented by Broche et al. (1983), $F(x, \alpha) \simeq F(x, 0) \cos \alpha$, with the largest errors occurring for $x = 1$ where $F(x, \alpha) > F(x, 0) \cos \alpha$ for $|\alpha| < \pi/3$, which, in our case makes U_{Sf} larger by 2 to 5% than the approximation given by eq. (5).

APPENDIX B Parameterization and numerical settings for the wave models

a. Parameterizations

The implementation of the WAVEWATCH III model used here was ran with source functions S_{in} , S_{nl} and S_{ds} parameterizing the wind input, nonlinear 4-wave interactions and whitecapping dissipation. An extra additional dissipation term S_{db} is also included to enhance the dissipation due to wave breaking in shallow water based on Battjes and Janssen (1978).

The parameterization for S_{nl} is taken from Hasselmann et al. (1985), with a minor reduction of the coupling coefficient from 2.78×10^7 to 2.5×10^7 . The parameterizations for S_{in} and S_{ds} are very similar

the ones used by Ardhuin et al. (2008b), with modifications to further improve the high frequency part of the spectrum (Filipot et al. 2008). Namely, the whitecapping dissipation is based on recent observations of wave breaking statistics (Banner et al. 2000), and swell dissipation (Ardhuin et al. 2009a). These model settings give the best estimates so far of wave heights, peak and mean periods, but also of parameters related to the high frequency tail of the spectrum (appendix C). The present model results are thus a significant improvement over the results of Bidlot et al. (2005) and Rascle et al. (2008). The physical and practical motivations for the parameterizations will be fully described elsewhere, and we only give here a description of their implementation. We only note for the interested users, that the parameter settings given here tend to produce larger negative biases on H_s for $H_s > 8$ m than the parameterization by Bidlot et al. (2005). Better settings for H_s in extreme waves would be $s_u = 0$ and $c_3 = 0.5$ (see below), but this tends to give too large values of U_{ss} , which is why we do not use these settings here.

The parameterization of S_{in} is taken from Janssen (1991) as modified by Bidlot et al. (2005), with some further modifications for the high frequencies, and the addition of a wind output term S_{out} (or "negative wind input") based on the observations by Ardhuin et al. (2009a). The source term is thus

$$\begin{aligned} S_{in}(f, \theta) &= \frac{\rho_a}{\rho_w} \frac{\beta_{\max}}{\kappa^2} e^Z Z^4 \left(\frac{u'_*}{C} + z_\alpha \right)^2 \\ &\times \cos^2(\theta - \theta_u) \sigma F(f, \theta) + S_{out}(f, \theta), \end{aligned} \quad (\text{B1})$$

where β_{\max} is a (constant) non-dimensional growth parameter, κ is von Kármán's constant, u_* in the friction velocity in the air, C is the phase speed of the waves, σ is the intrinsic frequency, equal to $2\pi f$ in the absence of currents, and $F(f, \theta)$ is the frequency-directional spectrum of the surface elevation variance. In the present implementation the air/water density ratio is constant. We define $Z = \log(\mu)$ where μ is given by Janssen (1991, eq. 16), corrected for intermediate water depths, so that

$$Z = \log(kz_1) + \kappa / [\cos(\theta - \theta_u) (u'_* + z_\alpha)], \quad (\text{B2})$$

where z_1 is a roughness length modified by the wave-supported stress τ_w , and z_α is a wave age tuning parameter. The effective roughness z_1 is implicitly defined by

$$U_{10} = \frac{u_*}{\kappa} \log \left(\frac{10 \text{ m}}{z_1} \right) \quad (\text{B3})$$

$$z_0 = \max \left\{ \alpha_0 \frac{u_*^2}{g}, 0.0020 \right\} \quad (\text{B4})$$

$$z_1 = \frac{z_0}{\sqrt{1 - \tau_w/\tau}}, \quad (\text{B5})$$

where τ is the wind stress magnitude, τ_w is the wave-supported fraction of the wind stress, U_{10} is the wind at

10 m height and g is the acceleration of gravity.

The maximum value of z_0 was added to reduce the unrealistic stresses at high winds that are otherwise given by the standard parameterization. This is equivalent to setting a maximum wind drag coefficient of 2.8×10^{-3} . This, together with the use of an effective friction velocity $u'_*(f)$ instead of u_* in (B2) are the only changes to the general form of Janssen's (1991) wind input. That friction velocity is defined by

$$(u'_*(f))^2 = |u_*^2 e_\theta - |s_u| \int_0^f \int_0^{2\pi} \frac{S_{in}(f', \theta')}{C} e_\theta df' d\theta'|, \quad (\text{B6})$$

Here the empirical factor $s_u = 1.0$ adjusts the sheltering effect of short waves by long waves adapted from Chen and Belcher (2000), and helps to reduce the input at high frequency, without which a balance of source terms would not be possible (except with a very high dissipation as in Bidlot et al. 2005). This sheltering is also applied in the precomputed tables that gives the wind stress as a function of U_{10} and τ_w/τ (Bidlot et al. 2005).

The wind output term, is identical to the one used by Ardhuin et al. (2008b). Namely, defining the Reynolds number $\text{Re} = 4u_{\text{orb}}a_{\text{orb}}/\nu_a$, where u_{orb} and a_{orb} are the significant surface orbital velocity and displacement amplitudes, and ν_a is the air viscosity, we take, for $\text{Re} < 10^5$

$$S_{\text{out}}(f, \theta) = -1.2 \frac{\rho_a}{\rho_w} \left\{ 2k\sqrt{2\nu\sigma} \right\} F(f, \theta). \quad (\text{B7})$$

and otherwise

$$S_{\text{out}}(f, \theta) = -\frac{\rho_a}{\rho_w} \left\{ 16f_e \sigma^2 u_{\text{orb}}/g \right\} F(f, \theta), \quad (\text{B8})$$

where

$$f_e = 0.7f_{e,GM} + [0.015 - 0.018 \cos(\theta - \theta_u)] u_*/u_{\text{orb}}, \quad (\text{B9})$$

where $f_{e,GM}$ is the friction factor given by Grant and Madsen's (1979) theory for rough oscillatory boundary layers without a mean flow, using a roughness length adjusted to 0.04 times the roughness for the wind. This gives a stronger dissipation for swells opposed to winds.

The dissipation term is the sum of the saturation-based term of Ardhuin et al. (2008b) and a cumulative breaking term $S_{\text{ds,c}}$ of Filipot et al. (2008). It thus takes the form

$$S_{\text{ds}}(f, \theta) = \sigma C_{\text{ds}} \left\{ 0.25 \left[\max \left\{ \frac{B(f)}{B_r} - 1, 0 \right\} \right]^2 + 0.75 \left[\max \left\{ \frac{B'(f, \theta)}{B_r} - 1, 0 \right\} \right]^2 \right\} \times F(f, \theta) + S_{\text{ds,c}}(f, \theta). \quad (\text{B10})$$

where

$$B'(f, \theta) = \int_{\theta-80^\circ}^{\theta+80^\circ} k^3 \cos^2(\theta - \theta') F(f, \theta') C_g / (2\pi) d\theta', \quad (\text{B11})$$

$$B(f) = \max \{ B'(f, \theta), \theta \in [0, 2\pi] \}, \quad (\text{B12})$$

and $B_r = 0.0009$ is a threshold for the onset of breaking consistent with the observations of Banner et al. (2000) and Banner et al. (2002), as discussed by Babanin and van der Westhuysen (2008), when including the normalization by the width of the directional spectrum (here replaced by the \cos^2 factor in eq. B11).

The dissipation constant C_{ds} was adjusted to 2.2×10^{-4} in order to reproduce the directional fetch-limited data described by Ardhuin et al. (2007).

The cumulative breaking term represents the smoothing of the surface by big breakers with celerity C' that wipe out smaller waves of phase speed C (Babanin and Young 2005). Due to uncertainties in the estimation of this effect from observations, we use the theoretical model of Filipot et al. (2008). Briefly, the relative velocity of the crests is the norm of the vector difference, $\Delta_C = |C - C'|$, and the dissipation rate of short wave is simply the rate of passage of the large breaker over short waves, i.e. the integral of $\Delta_C \Lambda(C) dC$, where $\Lambda(C) dC$ is the length of breaking crests per unit surface that have velocity components between C_x and $C_x + dC_x$, and between C_y and $C_y + dC_y$ (Phillips 1985). Because there is no consensus on the form of Λ (Gemmrich et al. 2008), we prefer to link Λ to breaking probabilities. Based on Banner et al. (2000, figure 6), and taking their saturation parameter ε to be of the order of $1.6\sqrt{B}$, the breaking probability of dominant waves waves is approximately $P = 56.8 \left(\max \{ \sqrt{B} - \sqrt{B_r}, 0 \} \right)^2$. Extrapolating this result to higher frequencies, and assuming that the spectral density of crest length per unit surface $l(\mathbf{k})$, in the wavenumber spectral space, is $l(\mathbf{k}) = 1/(2\pi^2 k)$, we define a spectral density of breaking crest length, $\Lambda(\mathbf{k}) = l(\mathbf{k})P(\mathbf{k})$, giving the source term,

$$S_{\text{ds,c}}(f, \theta) = -c_3 F(f, \theta) \int_0^{0.7f} \int_0^{2\pi} \frac{56.3}{\pi} \times \max \left\{ \sqrt{B(f', \theta')} - \sqrt{B_r}, 0 \right\} \frac{\Delta_C}{C_g} d\theta' df' \quad (\text{B13})$$

The tuning coefficient c_3 which was expected to be of order 1, was here adjusted to 0.2. The resulting model results appear to be very accurate for sea states with significant wave heights up to 8 m. Larger wave heights are underestimated. Other parameter adjustments can correct for this defect, e.g. reducing s_u and increasing c_3 , but then the Stokes drift may not be so well reproduced, especially for the average conditions discussed here. These different possible adjustments and their effects will be discussed elsewhere.

b. Numerical schemes and model settings

Spatial advection in the finer model grid is performed using the explicit CRD-N scheme (Contour integration based Residual Distribution - Narrow stencil scheme Csík et al. 2002) that was applied to the Wave Action Equation by Roland (2008) and provided as a module for the WWIII model. The scheme is first order in time and space, it is conservative and monotone.

All model grids are forced by 6-hourly wind analysis at 0.5 degree resolution, provided by ECMWF. The model spectral grid has 24 regularly spaced directions, and extends from 0.037 to $f_{\max} = 0.72$ Hz with 32 frequencies exponentially spaced. The model thus covers the full range of frequencies that contribute most to the filtered Stokes drift U_{Sf} . The usual high frequency tail proportional to f^{-5} is only imposed for frequencies larger than the diagnostic frequency $f_d = F f_{m,0,-1}$, with the mean frequency defined by $f_{m,0,-1} = [\int E(f)/f df / \int E(f) df]^{-1}$. Here we take a factor $F = 10$, instead of the usual value of 2.5 (Bidlot et al. 2005), so that f_d is almost always larger than the model maximum frequency of 0.72 Hz. Besides, the time step for integration of the source function is adaptatively refined from 150 s for the local model down to 10 s if needed, so that virtually no limiter constrains the wave field evolution (Tolman 2002).

APPENDIX C Model accuracy for relevant parameters

In order to define the errors on the estimations of U_{Sf} used to determine the quasi-Eulerian velocity U_E from the radar measurement, it is necessary to examine the quality of the wind forcing and model results in the area of interest. The only two parameters that are measured continuously offshore of the area of interest are the wave height H_s and mean period f_{02} , recorded at buoy 62163, 150 km to the west of point A. H_s and f_{02} can be combined to give the second moment of the wave spectrum $m_2 = (0.25 H_s f_{02})^2$.

Because there is no reliable wave measurement with spectral information in deep water off the French North-East Atlantic coast, we also use buoy data and model result in a relatively similar wave environment, at the location of buoy 46005, 650 km off Aberdeen (WA), on the U.S. Pacific coast. Since this buoy is not directional we first examine the third moment of the wave spectrum

$$m_3(f_c) = \int_0^{f_c} f^3 E(f) df. \quad (C1)$$

If waves were all in the same direction, m_3 would be proportional to the Stokes drift $U_{ss}(f_c)$ of waves with frequency up to f_c , as given by eq. (4). We thus define a non-directional Stokes drift

$$U_{ssnd}(f_c) = (2\pi)^3 m_3(f_c) / g. \quad (C2)$$

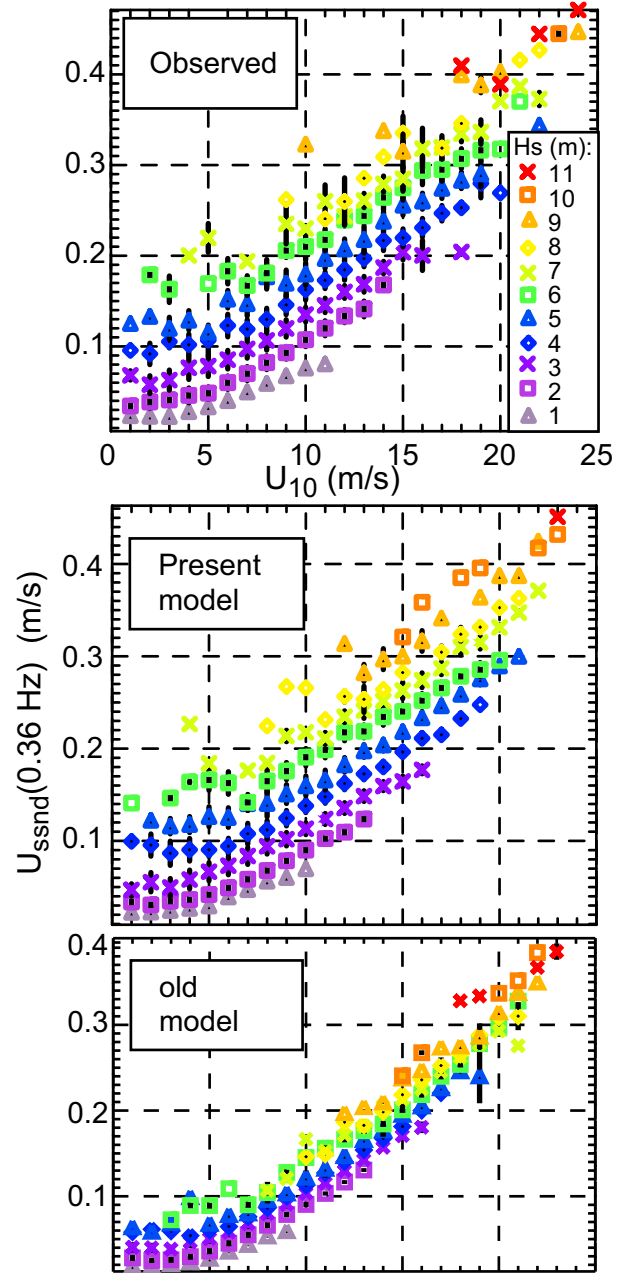


FIG. C1. Variation of the wave spectrum third moment, m_3 converted to a velocity $U_{ssnd} = (2\pi)^3 m_3(f_c) / g$, that would equal the surface Stokes drift in deep water if all waves propagated in the same direction. For each data source a cut-off frequency of $f_c = f_B = 0.36$ Hz is taken and the data is binned wind speed, at 1 m s^{-1} intervals, and significant wave height H_s (in colors) at 1 m intervals from 1 to 11 m. The top panel shows buoy data offshore of Oregon (NDBC buoy 46005), the middle panel shows present model results, and the bottom panel shows results from the same model but using the parameterization of Bidlot et al. (2005), including a factor $F = 2.5$. The vertical error bars indicate plus and minus half the standard deviation of the data values in each (U_{10}, H_s) class.

Looking at buoy data we found that

$$U_{ssnd}(f_c) \simeq 5.9 \times 10^{-4} \left[1.25 - 0.25 \left(\frac{0.5}{f_c} \right)^{1.3} \right] U_{10} \times \min \{U_{10}, 14.5\} + 0.027 (H_s - 0.4), \quad (C3)$$

where f_c is in Hertz, U_{10} is in meters per second, and H_s is in meters.

Taking directionality into account eq. (4) yields $U_{ss}(f_c) \simeq 0.85 U_{ssnd}(f_c)$, for typical wave spectra, and the relationship (C3) becomes eq. (7). For buoy 46005, which is a 6 m NOMAD buoy, and f_c in the range 0.3 to 0.5 Hz, this relationship gives a root mean square (r. m. s.) error less than 1.0 cm s^{-1} , corresponding to less than 15% of the r. m. s. value estimated using eq. (C2). This is smaller than the error of estimates using previous wave models (24% with the parameterization by Bidlot et al. 2005), but comparable to the 14.2% error obtained with the present model. The same analysis was performed, with similar results, for very different sea states recorded by NDBC buoys 51001 (North-East of Hawaii), 41002 (U.S. East coast), 46047 (Tanner Banks, California), and 42036 (Gulf of Mexico).

Another source of continuous wave measurements is provided by altimeter-derived H_s , which we correct for bias following Queffelec (2004), and fourth spectral moment m_4 . The latter is approximately given by (Vandemark et al. 2004)

$$m_4 = \frac{0.64g^2}{(2\pi)^4\sigma_0}, \quad (C4)$$

where σ_0 is the normalized radar cross-section, corrected for a 1.2 dB bias on the C-band altimeter of JASON in order to fit airborne observations (Hauser et al. 2008). The model estimation of m_4 (0.72 Hz) is extrapolated to C-band by the addition of a constant $0.011g^2/(2\pi)^4$, consistent with the saturation of the short wave slopes observed by Vandemark et al. (2004). For this parameter, the model is found to be very accurate, especially around the region of interest, relatively more than on the U.S. Pacific coast.

These indirect validations suggest that the third spectral moment including waves up to the Bragg frequency $f_B = 0.36 \text{ Hz}$, which is proportional to U_{ssnd} , is probably estimated with bias between -5 and 10%, and an r.m.s. error less than 20%. The bias on the significant wave height appears to increase from offshore (altimeter and buoy 62163 data), to the coast (buoys Iroise and 62069), and we attribute this effect to the tidal currents, not included in the present wave model, and coastal modifications of the winds that are not well reproduced at this 10-20 km scale by the ECMWF model. Because the chosen area of interest lies offshore of the area where currents are strongest (figure 1), we shall assume that, at this site, the model bias on $U_{ss}(f_B)$ is zero, which appears

Table C1. Model accuracy for measured wave parameters in various regions of the world ocean. Buoy validation span the entire year 2007, except for buoy 62069 for which data covers the time frame 25 January to 20 August 2008, buoy Iroise covers 13 April to 20 May 2004, and JASON 1 data corresponds to January to July 2007 for the global validation (JAS-Glo: 393382 data points) and the full year for a box 3° by 4° centered on 48.5° N and 8° W or 45° N and 128° W . (JAS-Gas or JAS-Was: 380 data points). Unless otherwise specified by the number in parenthesis, the cut-off frequency is taken to be 0.5 Hz, C stands for C-band and $f_B = 0.36 \text{ Hz}$ corresponds to our 12 MHz HF radar. The normalized bias (NB) is defined as the bias divided by the r.m.s. observed value, while the scatter index (SI) is defined as the r.m.s. difference between modeled and observed values, after correction for the bias, normalized by the r.m.s. observed value, and r is Pearson's correlation coefficient. Only altimeter data are available at point A but the uniform error pattern and the model consistency suggest that errors at A should be similar to offshore buoy errors such as found at buoy 62163 offshore of A, or at the U.S. West coast buoy 46005. Errors at point B, not discussed here, are expected to be closer to those at the nearshore buoys 62069 and Iroise.

| | dataset | NB(%) | SI(%) | r |
|-----------------|---------|-------|-------|-------|
| 2004 | | | | |
| H_s | 62163 | 6.8 | 11.1 | 0.977 |
| f_{02} | 62163 | 10.4 | 8.8 | 0.907 |
| H_s | Iroise | 12.8 | 17.4 | 0.975 |
| f_{02} | Iroise | -10.0 | 11.7 | 0.913 |
| $U_{ssnd}(f_B)$ | Iroise | 27.2 | 26.9 | 0.968 |
| $U_{ss}(f_B)$ | Iroise | 20.5 | 18.5 | 0.971 |
| 2007/2008 | | | | |
| H_s | JAS-Glo | -0.6 | 11.4 | 0.966 |
| $m_4(C)$ | JAS-Glo | 0.6 | 9.1 | 0.939 |
| H_s | 62163 | -1.4 | 8.8 | 0.985 |
| f_{02} | 62163 | 6.3 | 7.3 | 0.938 |
| H_s | 62069 | 10.1 | 14.1 | 0.974 |
| f_{02} | 62069 | -7.7 | 11.8 | 0.886 |
| $m_4(f_B)$ | 62069 | 15.8 | 24.1 | 0.955 |
| $U_{ssnd}(f_B)$ | 62069 | 13.9 | 23.0 | 0.965 |
| $U_{ss}(f_B)$ | 62069 | 11.1 | 21.0 | 0.963 |
| H_s | JAS-Gas | -2.6 | 8.8 | 0.983 |
| $m_4(C)$ | JAS-Gas | 1.0 | 6.7 | 0.962 |
| H_s | 46005 | 4.9 | 10.2 | 0.975 |
| f_{02} | 46005 | -2.8 | 6.6 | 0.931 |
| $m_4(f_B)$ | 46005 | -5.4 | 13.5 | 0.965 |
| $U_{ssnd}(f_B)$ | 46005 | -4.9 | 12.6 | 0.973 |
| $U_{ssnd}(0.5)$ | 46005 | 6.2 | 12.7 | 0.971 |
| H_s | JAS-Was | 2.4 | 7.9 | 0.985 |
| $m_4(C)$ | JAS-Was | 1.8 | 7.3 | 0.953 |

most likely, or possibly weakly negative. Extreme biases of $\pm 10\%$ only result in deflections of 5 degrees on the diagnosed quasi-Eulerian current U_E .

REFERENCES

- Agrawal, Y. C., E. A. Terray, M. A. Donelan, P. A. Hwang, A. J. Williams, W. Drennan, K. Kahma, and S. Kitaigorodskii, 1992: Enhanced dissipation of kinetic energy beneath breaking waves. *Nature*, **359**, 219–220.
- Arduin, F., 2006: Quelles mesures pour la prévision des états de mer en zone côtière? *Communications de l'Atelier Experimentation et*

- boundary layer. *J. Phys. Oceanogr.*, **7**, 248–255.
- Mao, Y. and M. L. Heron, 2008: The influence of fetch on the response of surface currents to wind studied by HF ocean surface radar. *J. Phys. Oceanogr.*, **38**, 1107–1121.
<http://ams.allenpress.com/archive/1520-0485/38/5/pdf/i1520-0485-38-5-639.pdf>
- Mariette, V. and B. Le Cann, 1985: Simulation of the formation of the Ushant thermal front. *Continental Shelf Research*, **4**, 637.
- Mellor, G. and A. Blumberg, 2004: Wave breaking and ocean surface layer thermal response. *J. Phys. Oceanogr.*, **34**, 693–698.
- Millot, C. and M. Crépon, 1981: Inertial oscillations on the continental shelf of the Gulf of Lions— observations and theory. *J. Phys. Oceanogr.*, **11**, 639–657.
<http://ams.allenpress.com/archive/1520-0485/11/5/pdf/i1520-0485-11-5-639.pdf>
- Nerheim, S. and A. Stigebrandt, 2006: On the influence of buoyancy fluxes on wind drift currents. *J. Phys. Oceanogr.*, **36**, 1591–1604.
- Pawlowicz, R., B. Beardsley, and S. Lentz, 2002: Classical tidal harmonic analysis including error estimates in MATLAB using T.TIDE. *Computers and Geosciences*, **28**, 929–937.
- Phillips, O. M., 1985: Spectral and statistical properties of the equilibrium range in wind-generated gravity waves. *J. Fluid Mech.*, **156**, 505–531.
- Pollard, R. T., 1983: Observations of the structure of the upper ocean: Wind-driven momentum budget. *Phil. Trans. Roy. Soc. London A*, **380**, 407–425.
- Polton, J. A., D. M. Lewis, and S. E. Belcher, 2005: The role of wave-induced Coriolis-Stokes forcing on the wind-driven mixed layer. *J. Phys. Oceanogr.*, **35**, 444–457.
- Prandle, D., 1987: The fine-structure of nearshore tidal and residual circulations revealed by H. F. radar surface current measurements. *JPO*, **17**, 231–245.
<http://ams.allenpress.com/archive/1520-0485/17/2/pdf/i1520-0485-17-2-231.pdf>
- Price, J. F. and M. A. Sundermeyer, 1999: Stratified Ekman layers. *J. Geophys. Res.*, **104**, 20467–20494.
- Queffelecoulou, P., 2004: Long term validation of wave height measurements from altimeters. *Marine Geodesy*, **27**, 495–510, doi: 10.1080/01490410490883478.
- Rasclé, N., 2007: *Impact of waves on the ocean circulation (Impact des vagues sur la circulation océanique)*. Ph.D. thesis, Université de Bretagne Occidentale, available at <http://tel.archives-ouvertes.fr/tel-00182250/>.
<http://tel.archives-ouvertes.fr/tel-00182250/>
- Rasclé, N. and F. Ardhuin, 2009: Drift and mixing under the ocean surface revisited. stratified conditions and model-data comparisons. *J. Geophys. Res.*, **114**, in press, doi:10.1029/2007JC004466.
- Rasclé, N., F. Ardhuin, P. Queffelecoulou, and D. Croizé-Fillon, 2008: A global wave parameter database for geophysical applications. part 1: wave-current-turbulence interaction parameters for the open ocean based on traditional parameterizations. *Ocean Modelling*, **25**, 154–171, doi:10.1016/j.ocemod.2008.07.006.
<http://hal.archives-ouvertes.fr/hal-00201380/>
- Rasclé, N., F. Ardhuin, and E. A. Terray, 2006: Drift and mixing under the ocean surface. a coherent one-dimensional description with application to unstratified conditions. *J. Geophys. Res.*, **111**, C03016, doi:10.1029/2005JC003004.
- Rio, M.-H. and F. Hernandez, 2003: High-frequency response of wind-driven currents measured by drifting buoys and altimetry over the world ocean. *J. Geophys. Res.*, **108**, 3283, doi:10.1029/2002JC001655.
- Roland, A., 2008: *Development of WWM II: Spectral wave modelling on unstructured meshes*. Ph.D. thesis, Technische Universität Darmstadt, Institute of Hydraulic and Water Resources Engineering.
- Santala, M. J. and E. A. Terray, 1992: A technique for making unbiased estimates of current shear from a wave-follower. *Deep Sea Res.*, **39**, 607–622.
<http://ams.allenpress.com/archive/1520-0485-39-607-622.pdf>
- Shay, L. K., J. Martinez-Pedraja, T. M. Cook, and B. K. Haus, 2007: High-frequency radar mapping of surface currents using WERA. *J. Atmos. Ocean Technol.*, **112**, 484–503.
- Smith, J. A., 2006: Wave-current interactions in finite-depth. *J. Phys. Oceanogr.*, **36**, 1403–1419.
- Stewart, R. H. and J. W. Joy, 1974: HF radio measurements of surface currents. *Deep Sea Res.*, **21**, 1039–1049.
- Terray, E. A., M. A. Donelan, Y. C. Agrawal, W. M. Drennan, K. K. Kahma, A. J. Williams, P. A. Hwang, and S. A. Kitaigorodskii, 1996: Estimates of kinetic energy dissipation under breaking waves. *J. Phys. Oceanogr.*, **26**, 792–807.
- Tolman, H. L., 2002: Limiters in third-generation wind wave models. *Global Atmos. Ocean Syst.*, **8**, 67–83.
- 2007: The 2007 release of WAVEWATCH III. *Proceedings, 10th Int. Workshop of Wave Hindcasting and Forecasting, Hawaii*.
http://www.waveworkshop.org/10thWaves/Papers/oahu07_Q4.pdf
- 2008: A mosaic approach to wind wave modeling. *Ocean Modelling*, **25**, doi:10.1016/j.ocemod.2008.06.005, 35–47.
- Vandemark, D., B. Chapron, J. Sun, G. H. Crescenti, and H. C. Graber, 2004: Ocean wave slope observations using radar backscatter and laser altimeters. *J. Phys. Oceanogr.*, **34**, 2825–2842.
- Wang, W. and R. X. Huang, 2004: Wind energy input to the surface waves. *J. Phys. Oceanogr.*, **34**, 1276–1280.
<http://ams.allenpress.com/archive/1520-0485/34/5/pdf/i1520-0485-34-5-1276.pdf>
- Weber, B. L. and D. E. Barrick, 1977: On the nonlinear theory for gravity waves on the ocean's surface. Part I: Derivations. *J. Phys. Oceanogr.*, **7**, 3–10.
<http://ams.allenpress.com/archive/1520-0485/7/1/pdf/i1520-0485-7-1-3.pdf>
- Xu, Z. and A. J. Bowen, 1994: Wave- and wind-driven flow in water of finite depth. *J. Phys. Oceanogr.*, **24**, 1850–1866.
<http://ams.allenpress.com/archive/1520-0485/24/9/pdf/i1520-0485-24-9-1850.pdf>

Fabrice's Draft: January 21, 2020

Generated with ametsocjmk.cls.

Written by J. M. Klymak

mailto:jklymak@ucsd.edu

<http://opgl.ucsd.edu/~jklymak/WorkTools.html>